arXiv:1408.1418v2 [cond-mat.str-el] 23 Oct 2014

Theory of the evolution of magnetic order in $Fe_{1+y}Te$ compounds with increasing interstitial iron

Samuel Ducatman,[1,2] Rafael M. Fernandes,[2] and Natalia B. Perkins[1,2]

[1]*Department of Physics, University of Wisconsin-Madison, Madison, WI 53706, USA*
[2]*School of Physics and Astronomy, University of Minnesota, Minneapolis, MN 55455, USA*

We examine the influence of the excess of interstitial Fe on the magnetic properties of $Fe_{1+y}Te$ compounds. Because in iron chalcogenides the correlations are stronger than in the iron arsenides, we assume in our model that some of the Fe orbitals give rise to localized magnetic moments. These moments interact with each other via exchange interactions as well as phonon-mediated biquadratic interactions that favor a collinear double-stripe state, corresponding to the ordering vectors $(\pm\pi/2, \pm\pi/2)$. The remaining Fe orbitals are assumed to be itinerant, giving rise to the first-principle derived Fermi surface displaying nesting features at momenta $(\pi, 0) / (0, \pi)$. Increasing the amount of itinerant electrons due to excess Fe, y, leads to changes in the Fermi surface and to the suppression of its nesting properties. As a result, due to the Hund's coupling between the itinerant and localized moments, increasing y leads to modifications in the local moments' exchange interactions via the multi-orbital generalization of the long-range Ruderman-Kittel-Kasuya-Yosida (RKKY) interaction. By numerically computing the RKKY corrections and minimizing the resulting effective exchange Hamiltonian, we find, in general, that the excess electrons introduced in the system change the classical magnetic ground state from a double-stripe state to an incommensurate spiral, consistent with the experimental observations. We show that these results can be understood as a result of the suppression of magnetic spectral weight of the itinerant electrons at momenta $(\pi, 0) / (0, \pi)$, combined with the transfer of broad magnetic spectral weight from large to small momenta, promoted by the introduction of excess Fe.

I. INTRODUCTION

$Fe_{1+y}Te$ chalcogenides are the parent compounds of the simplest family of iron-based superconductors.[1–13] Both the electronic and magnetic properties of $Fe_{1+y}Te$ compounds show strong sensitivity to the amount of non-stoichiometric Fe ions. For small values of y, the low-temperature crystal structure is monoclinic ($P21/m$), and the magnetic order is described by the commensurate propagation vector $\mathbf{Q} = (\pm\pi/2, \pm\pi/2)$, corresponding to a double-stripe pattern. This is remarkably different from FeAs-based parent compounds, which display an antiferromagnetic order described by $\mathbf{Q} = (\pi, 0)$ or $\mathbf{Q} = (0, \pi)$, corresponding to single-stripe patterns, and a crystal structure with orthorhombic symmetry ($Pmmn$). Experimentally, it is observed that by increasing the amount of interstitial Fe, the magnetic structure of $Fe_{1+y}Te$ becomes an incommensurate spiral. The incommensurate ordering manifests itself as a shift in the elastic neutron scattering peak with respect to the $\mathbf{Q} = (\pm\pi/2, \pm\pi/2)$ positions. According to neutron scattering experiments,[1,5–7,12,13] in the range of $0.11 < y < 0.16$ the shift is approximately along the diagonal directions $\mathbf{Q} = (\pi/2 - \delta, \pi/2 - \delta)$ or $\mathbf{Q} = (-\pi/2 + \delta, \pi/2 - \delta)$; however, δ does not vary smoothly with y.

There have been several theoretical attempts to understand the magnetic properties of $Fe_{1+y}Te$ compounds within the localized spin scenario,[14–18] since these materials are known to be more strongly correlated than their arsenide counterparts.[19] Although the magnetic order at both low and at high levels of Fe excess can be successfully described by a $J_1 - J_2 - J_3$ super-exchange model, it is clear that the local picture alone cannot describe the magnetic properties of $Fe_{1+y}Te$, as it requires y-dependent exchange couplings. Alternatively, this property indicates that itinerant electrons are also important to describe the magnetism of these materials, suggesting that hybrid models with coupled localized-itinerant moments are a suitable starting point.[20–26]

In this paper, we argue that the evolution of the magnetic interactions due to y-dependent charge doping is the key to understand the experimentally observed magnetic phase diagram of $Fe_{1+y}Te$. Our study is based on the assumption that, in these particular iron chalcogenides, some of the Fe orbitals are almost localized while the other orbitals remain itinerant. This idea is supported by recent dynamical mean-field theory studies of FeTe systems[27,28] showing that the Hund's coupling can promote an orbital-selective localization already in the paramagnetic phase.[29] Here, we demonstrate that the change in magnetic properties observed in the $Fe_{1+y}Te$ compounds can be reasonably well captured by an effective model in which localized spins acquire a long-range RKKY-type interaction,[30–32] in addition to the $J_1 - J_2 - J_3$ Heisenberg super-exchange[14] and biquadratic couplings.[33–37] We note that in Refs.[33,34] the biquadratic term was calculated on a purely electronic basis, and obtained model gave a good agreement with experimentally measured spin-wave spectrum in several Fe-based materials. Another possible origin of the biquadratic terms is due to the magnetoelastic coupling.[35–37]

The former, mediated by the multi-orbital spin susceptibility of the itinerant electrons, is sensitive to the addition of excess Fe y, rendering the magnetic ground state of the local spins change as a function of y. In particular, we find that the shift in the chemical potential

promoted by the excess electrons changes the Fermi surface in a way that suppresses the $(\pi,0)\,/\,(0,\pi)$ peaks of the itinerant spin susceptibility of the parent compound, promoting at the same time peaks at small-momentum values. As a result, the effective exchange interaction J_2 is suppressed, J_3 is enhanced, and J_1 changes sign, favoring a spiral incommensurate state, in contrast to the double-stripe state of the stoichiometric compound.

The outline of the paper is as follows. In Sec. II, we present an effective super-exchange model describing localized magnetic moments in the multi-band correlated electron sea and argue that this is a suitable minimal microscopic model to describe the magnetism of $Fe_{1+y}Te$ compounds. In Sec. III, we study the evolution of the Fermi surface of $FeTe_{1+y}$ with increasing level of the Fe excess using the tight-binding model (TBM) originally proposed by Ma *et al*[14], which had been later also used by Wang *et al*[38] to explain further resutls in $FeTe_{1+y}$. We show that while the Fermi surface at small y has both small hole pockets at the Γ- and M-points and elliptical electron pockets at the X- and Y-points, at large y all pockets are electron-like. In Sec. IV, we study spin fluctuations in the correlated multi-band electron system and compute the Pauli susceptibility within the random phase approximation (RPA). We find that at small y the itinerant spin susceptibility peaks at $(\pi,0)$ and $(0,\pi)$ due to the weak nesting between the hole and the electron pockets connected by these momenta. The y-dependent charge doping suppresses the $(\pi,0)$ and $(0,\pi)$ peaks, but it leads to an increase of the spin fluctuation in the central part of the Brillouin zone. In Sec. V, we compute the RKKY interactions. We first perform a qualitative computation of the RKKY interactions using a simple phenomenological model, and then perform a quantitative analysis based on the realistic RPA susceptibility obtained in Sec. IV. In Sec. VI, the classical phase diagram of the effective spin model is presented. In agreement with experimental findings, the computed phase diagram displays a transition, above a certain level of Fe excess, from a commensurate double-stripe phase, characterized by the wave-vectors $\mathbf{Q} = (\pi/2, \pm\pi/2)$ or $\mathbf{Q} = (\pm\pi/2, \pi/2)$, to an incommensurate spiral (IC) phase characterized by the wave-vector $\mathbf{Q} = (q, q)$. We conclude with a summary in Sec. VII. The paper has two appendices. Appendix A contains the derivation of the biquadratic exchange couplings arising from the magneto-elastic coupling. Appendix B provides the explicit expression of the classical energy of the effective super-exchange model describing $FeTe_{1+y}$.

II. THE MODEL

To capture the fact that in $Fe_{1+y}Te$ correlations lead to different levels of itineracy in distinct Fe orbitals,[27,28] we consider a semi-phenomenological "hybrid" model containing both localized and itinerant moments – similar in spirit to the models of Refs.[22–24]. In particular, we assume that the electrons occupying the x^2-y^2 and $3z^2-r^2$ orbitals form local moments with $S=1$ due to the Hund's coupling. The remaining $3d$ electrons have itinerant character and can be controlled by the concentration of excess Fe as y increases. A full derivation of such an effective model from the microscopic Hamiltonian is an intricate problem beyond the scope of this work.

In most of the paper, we assume that each excess Fe atom contributes eight electrons,[39] but our main conclusions do not change if one considers that less electrons are introduced by each Fe.[40,41] To account for the changes in the Fermi surface promoted by these excess Fe atoms, we employ a rigid band approximation in which the doping of excess electrons shifts the chemical potential from $\mu = 0$ to positive values.

Thus, the microscopic Hamiltonian we use is an effective double-exchange model describing localized magnetic moments in the multi-band correlated electron sea, which can be written as

$$H = H_e + H_{\mathbf{S}} + H_{\sigma\mathbf{S}} \ . \tag{1}$$

The first term describes the interacting itinerant electrons:

$$H_e = H_0 + H_{int}. \tag{2}$$

The non-interacting part H_0 is based on the five-orbital TBM

$$H_0 = \sum_{\mathbf{k},a,b,\sigma} \left(t^{ab}_{\mathbf{k}\sigma} c^\dagger_{\mathbf{k}a\sigma} c_{\mathbf{k}b\sigma} + H.C. \right) \ , \tag{3}$$

where $c^\dagger_{\mathbf{k}\sigma a}$ denotes the creation operator for an electron of momentum $\mathbf{k}$ with spin σ in the orbital a, and $t^{ab}_{\mathbf{k}\sigma}$ are the tight-binding matrix elements. Here, we are interested only in the contribution coming from the xz, yz, and xy orbitals, as explained above. Since the other orbitals do not contribute to the Fermi surface, the static spin susceptibility, which will give rise to the RKKY interactions, is very similar regardless of whether we consider a projected three-orbital model or the actual five-orbital tight-binding model.

The interaction part consists of four terms:[42–44]

$$\begin{aligned} H_{int} =& U \sum_{i,a} c^\dagger_{ia\uparrow} c_{ia\uparrow} c^\dagger_{ia\downarrow} c_{ia\downarrow} \\ &+ U' \sum_{i,a\neq b,\sigma,\sigma'} c^\dagger_{ia\sigma} c_{ia\sigma} c^\dagger_{ib\sigma'} c_{ib\sigma'} \\ &+ J_H \sum_{i,a\neq b,\sigma,\sigma'} c^\dagger_{ia\sigma} c^\dagger_{ib\sigma'} c_{ia\sigma'} c_{ib\sigma} \\ &+ J' \sum_{i,a\neq b} c^\dagger_{ia\uparrow} c^\dagger_{ia\downarrow} c_{ib\downarrow} c_{ib\uparrow} \end{aligned} \tag{4}$$

where U is the intra-orbital Coulomb repulsion, U' is the inter-orbital Coulomb repulsion, J_H is the Hund's coupling, and J' is the pair-hopping term. Hereafter, we

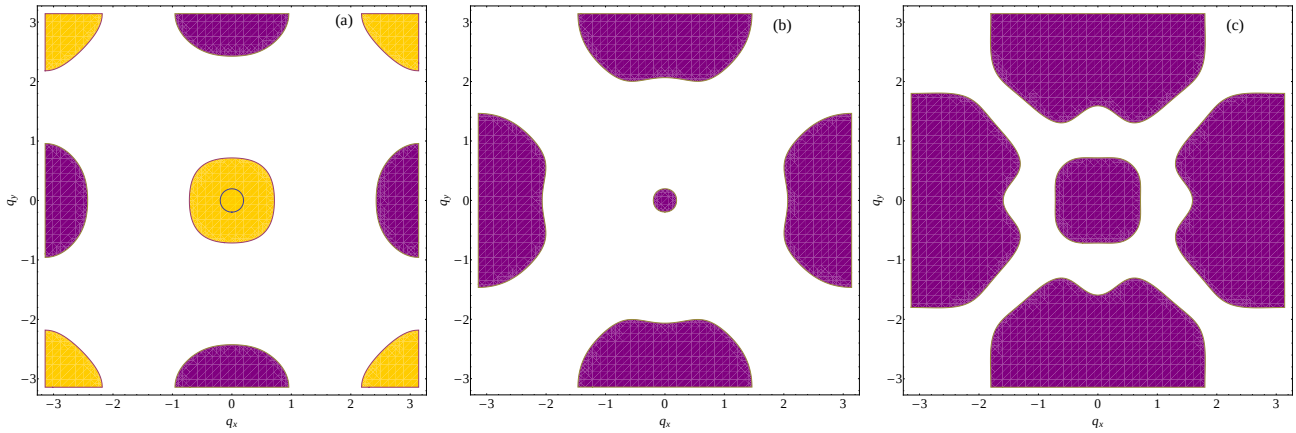

FIG. 1: Fermi surfaces of the TBM describing the itinerant electrons obtained for different values of the chemical potential μ: (a) $\mu = 0$ eV, (b) $\mu = 0.4$ eV, (c) $\mu = 0.8$ eV. The hole-like and the electron-like pockets are shown by yellow (light) and purple (dark) regions, correspondingly. The primary contribution to the electron pockets is from the xz and yz orbitals, whereas the hole pocket at the corner of the Brillouin zone is mainly of xy character.

set $U' = U - 2J_H$ and $J' = J_H$ to ensure the invariance of the Hamiltonian under rotations in orbital space.

The second term in Eq.(1) describes the interaction between the localized spins:

$$H_{\mathbf{S}} = \sum_{ij} \left(J_{ij} \mathbf{S}_i \cdot \mathbf{S}_j - \frac{K_{ij}}{S^2} (\mathbf{S}_i \cdot \mathbf{S}_j)^2 \right), \tag{5}$$

where J_1, J_2, and J_3 are super-exchange couplings between first-, second-, and third-nearest neighbors. In this work, we use the values of J_1, J_2, and J_3 obtained from the first-principles electronic-structure calculations.[14] K_{ij} denote generalized non-Heisenberg exchange couplings between first and second neighbors and ring-exchange. These couplings are predominantly determined by the magneto-elastic coupling, and their derivations are shown in Appendix A. In particular, here we consider the first- and second-neighbors biquadratic couplings K_1 and K_2, as well as a "diagonal" ring-exchange $K_{\rm diag} = -K_2$.

The third term

$$H_{\sigma \mathbf{S}} = J_H \sum_{j,a} \boldsymbol{\sigma}_{ja} \cdot \mathbf{S}_j \tag{6}$$

describes the coupling between the localized spins, $\mathbf{S}_j$, and the itinerant electrons $\boldsymbol{\sigma}_{ja}$. Here, $\mathbf{S}_j$ are the localized spins of electrons on orbitals $x^2 - y^2$ and $3z^2 - r^2$, and σ_{ja} are the spins of itinerant electrons on orbitals $a = xy, yz, xz$ defined as

$$\boldsymbol{\sigma}_{ja} = \frac{1}{N} \sum_{\mathbf{k},\mathbf{k}',\sigma,\sigma'} e^{i(\mathbf{k}'-\mathbf{k})\cdot\mathbf{R_j}} c^\dagger_{\mathbf{k}a\sigma} \boldsymbol{\tau}_{\sigma\sigma'} c_{\mathbf{k}'a\sigma'} \ , \tag{7}$$

where $\boldsymbol{\tau}_{\sigma\sigma'}$ are the Pauli matrices and N is the number of lattice sites. For our investigations, the sign of J_H is not important, as shown in the following. Due to the interaction described by Eq.(6), the itinerant electrons mediate additional exchange couplings between the localized moments:

$$H_{\rm RKKY} = \sum_{ij} J^{\rm RKKY}_{ij} \mathbf{S}_i \cdot \mathbf{S}_j. \tag{8}$$

The couplings $J^{\rm RKKY}_{ij}$ between localized spins on lattice sites $\mathbf{R}_i$ and $\mathbf{R}_j$, known as RKKY interactions, can be obtained by integrating out the itinerant degrees of freedom. In particular, $J^{\rm RKKY}_{ij}$ are determined by the static spin susceptibility $\chi(\mathbf{q}, \omega = 0) = \chi(\mathbf{q})$ of the multiband conduction electron sea:

$$\begin{aligned} J^{\rm RKKY}_{ij} \ = \ & - \ J_H^2 \chi(\mathbf{R}_i - \mathbf{R}_j) = \\ & - \ J_H^2 \sum_{\mathbf{q}} e^{\imath(\mathbf{R}_i - \mathbf{R}_j)\cdot\mathbf{q}} \chi(\mathbf{q}). \end{aligned} \tag{9}$$

Taking into account both Heisenberg and RKKY interactions, the effective low-energy Hamiltonian can then be written as

$$H_{\rm eff} = \sum_{ij} J^{\rm eff}_{ij} \mathbf{S}_i \mathbf{S}_j - \sum_{ij} \frac{K_{ij}}{S^2} (\mathbf{S}_i \cdot \mathbf{S}_j)^2, \tag{10}$$

where, for convenience, we defined $J^{\rm eff}_{ij} = J_{ij} + J^{\rm RKKY}_{ij}$.

III. FERMI SURFACE EVOLUTION

In this section, we discuss how the Fermi surface of $Fe_{1+y}Te$ evolves with increasing amount of interstitial Fe, y. To compute the Fermi surface, we use the TBM, those matrix elements we present in Table I.

TABLE I: Tight-binding hopping matrix elements of the TBM.[14,38] All $t_{ij}(\mathbf{R})$, where i, j are orbital indexes and $\mathbf{R}$ are distances between Fe ions, are given in eV. We use the following notations: $\mathbf{R} = (x, y)$, where $x = l_x a_x$, $y = l_y a_y$ and $\mathbf{a}$ is the unit vector of the one-Fe unit cell. Thus, (1,0) column corresponds to the hopping to the nearest neighbor in the x direction, (1,1) column corresponds to the hopping between second neighbors along the diagonal, etc. Last three columns define how the hopping elements change when one applies inversion symmetry (I), C_4 rotation which switches $x \to y$ and mirror plane symmetry which changes $y \to -y$, respectively. Also, the relation $t_{ij}(\mathbf{R}) = t_{ji}(-\mathbf{R})$ stands. For shortness, we denote orbital indexes we as $1 = 3z^2 - r^2$, $2 = xz$, $3 = yz$, $4 = xy$, $5 = x^2 - y^2$. The uniform energy shifts of the diagonal elements t_{ii} (not shown in the Table) are given by $\epsilon_1 = -0.449$, $\epsilon_2 = 0.111$, $\epsilon_3 = 0.111$, $\epsilon_4 = -0.077$, and $\epsilon_5 = -0.366$ (in eV).

t_{ij} \ **R**(x,y)	(1,0)	(1,1)	(2,0)	(2,1)	(2,2)	I	$x \to y$	$y \to -y$
t_{11}	0.0164	−0.033	−0.0131	0	−0.0154	t_{11}	t_{11}	t_{11}
t_{12}	−0.126	0	−0.0125	0	0	$-t_{12}$	$-t_{12}$	$-t_{13}$
t_{13}	0.126	−0.206	0.0125	−0.0178	−0.0262	$-t_{13}$	t_{13}	$-t_{12}$
t_{14}	0	0.0894	0	0	−0.0112	t_{14}	t_{14}	$-t_{14}$
t_{15}	−0.356	0	−0.0301	−0.0102	0	t_{15}	$-t_{15}$	t_{15}
t_{22}	−0.217	0.131	−0.0178	0.0132	−0.0119	t_{22}	t_{22}	t_{33}
t_{23}	0.12	0	0.0326	−0.0283	0	t_{23}	$-t_{23}$	t_{23}
t_{24}	0.207	0	0	0	0	$-t_{24}$	$-t_{24}$	t_{34}
t_{25}	−0.302	0.143	0	0	0	$-t_{25}$	t_{25}	$-t_{35}$
t_{33}	−0.217	0.376	−0.0178	−0.0394	0.0839	t_{33}	t_{33}	t_{22}
t_{34}	0.207	0.115	0	0.0221	−0.0129	$-t_{34}$	t_{34}	t_{24}
t_{35}	0.302	0	0	0.0349	0	$-t_{35}$	$-t_{35}$	$-t_{25}$
t_{44}	0.0305	0.0904	0.0103	−0.0181	−0.0292	t_{44}	t_{44}	t_{44}
t_{45}	0	0	0	0.0145	0	t_{45}	$-t_{45}$	$-t_{45}$
t_{55}	0.397	−0.0508	−0.0448	0	0.0213	t_{55}	t_{55}	t_{55}

In Fig. 1 (a), we show the Fermi surface of FeTe ($y = 0$) obtained from the TBM. Since the pockets have predominantly xz, yz, and xy character, we present the Fermi surface without projecting out the localized-spin orbitals x^2-y^2 and $3z^2-r^2$. Similar to most iron pnictide parent compounds, the Fermi surface is characterized by elliptical electron pockets at the $X = (\pi, 0)$ and $Y = (0, \pi)$ points and circular hole pockets centered at the $\Gamma = (0, 0)$ and $M = (\pi, \pi)$ points. We note a weak nesting between electron and hole pockets connected by the wave vectors $(\pi, 0)$ and $(0, \pi)$, but no Fermi surface nesting associated with the magnetic ordering vector $(\pm\pi/2, \pm\pi/2)$. This observation is in agreement with an angle-resolved photoemission (ARPES) study of the topology of the Fermi surface,[2] which also did not observe nesting corresponding to the magnetic ordering vector.

When the level of interstitial Fe increases, the chemical potential shifts up, and the geometry of the Fermi surface changes significantly. In Figs. 1 (b) and (c) we plot constant energy cuts which correspond to the chemical potential shifts (b) μ =0.4 eV and (c) μ =0.8 eV. The nesting between electron and hole pockets disappears very quickly as the sizes of the hole and electron pockets change significantly with the shift of the chemical potential μ. Initially, while the size of the electron pockets is enlarged, the size of the hole pockets is reduced. The hole pockets disappear completely at $\mu = 0.23$ eV. Then, at bigger shifts of μ, the pocket at the Γ point changes its character and becomes electron-like at $\mu = 0.3$ eV. This general behavior is also in agreement with ARPES measurements in electron-doped iron arsenides.[45]

In order to relate the shift of the chemical potential μ to the amount of excess iron y, in Fig.2 (a) we plot the dependence of μ on y for two cases, within the rigid band approximation: in the first case, each interstitial Fe adds eight electrons (purple line) and in the second case[39], each excess Fe atom has the same valence as the non-interstitial atoms, adding six electrons (orange line).[40,41] Of course, the general trends are the same, the differences being in the specific values of y correspondent to each chemical potential shift. For instance, a shift of 0.4 eV (Fig. 1 (b)) corresponds to $y = 0.07$ and $y = 0.09$, if we consider that each interstitial Fe adds eight and six electrons, respectively, whereas the shift of 0.8 eV (Fig. 1 (c)) corresponds to $y = 0.15$ and $y = 0.20$, respectively, for 8 and 6 electrons. Hereafter, all results are computed assuming that each interstitial iron adds 8 electrons into the band.

In Fig. 2 (b), we show how the electron occupation numbers for different orbitals depend on the concentration of excess Fe, y. We see that the occupations of the xz, yz, and xy orbitals change significantly, indicating that the charge doping due to the Fe excess goes predominantly to these orbitals. The occupations of the $x^2 - y^2$ and $3z^2 - r^2$ orbitals barely change with an increase of y, which is consistent with the fact that these orbitals do

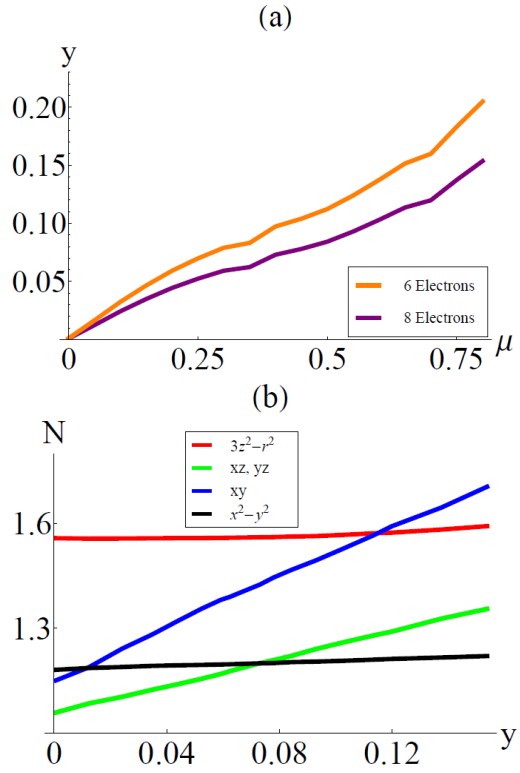

FIG. 2: (a) The dependence of the chemical potential shift μ on the concentration of excess iron y when each excess iron provides 6 electrons (orange) and 8 electrons (purple). (b) The orbitally resolved electron occupation numbers N as functions of y. The occupation of $3z^2-r^2$, xz, yz, xy, and x^2-y^2 orbitals are shown by red, green, brown, blue, and black lines, respectively. The xz and yz orbitals have the same electron occupation numbers due to the tetragonal symmetry of the system.

not contribute to the Fermi surface. Notice, that due to tetragonal symmetry, the occupation numbers of xz and yz orbitals are exactly the same and the corresponding lines completely overlap.

IV. SPIN SUSCEPTIBILITY OF ITINERANT ELECTRONS

Having established how the low-energy itinerant states change as a function of excess Fe, we now discuss in details the form of the multi-orbital spin susceptibility $\chi(\mathbf{q},\omega)$ as function of y. Here we use the formalism which was originally developed for the five-orbital model for the Fe-pnictides in Ref.[43] and later extensively studied for various orbital models in Ref.[46].

In the paramagnetic state, the spin-rotation invariance requires that transverse and longitudinal components of the spin susceptibility are identical. Thus, we can express $\chi(\mathbf{q},\omega)$ only in terms of the components of the transverse susceptibility: $\chi(\mathbf{q},\omega)=\frac{3}{2}\chi^{+-}(\mathbf{q},\omega)$. We note that as we are dealing with multi-orbital systems, the spin susceptibility is a four-index tensor, while the total susceptibility is a sum over all components of this tensor.

A. Bare susceptibility

In the multi-orbital model under consideration, the matrix elements of the bare spin susceptibility can be calculated from the corresponding Matsubara spin-spin correlation function of conduction electrons:

$$\chi^0_{aa'bb'}(\mathbf{q},\imath\nu_n) = -\frac{T}{N}\sum_{\mathbf{k},\imath\omega_n} G_{ab}(\mathbf{k},\imath\omega_n)G_{a'b'}(\mathbf{k}+\mathbf{q},\imath\omega_n+\imath\nu_n) \tag{11}$$

where a,a',b,b' are orbital indices, and the spectral representation of the multi-orbital Green's function is given by

$$G_{ab}(\mathbf{k},\imath\omega_n)=\sum_\nu \frac{u^a_\nu(\mathbf{k})(u^b_\nu(\mathbf{k}))^*}{\imath\omega_n - E_\nu(\mathbf{k})}\ . \tag{12}$$

Here, the matrix elements $u^a_\nu(\mathbf{k})$ are the components of the eigenvectors resulting from the diagonalization of the five-orbital TBM and $E_\nu(\mathbf{k})$ are the eigenvalues describing the resulting bands characterized by the band index ν. The retarded bare susceptibility is then obtained by summing over the Matsubara frequency and setting $\imath\nu_n\to\omega+\imath\delta$:

$$\chi^0_{aa'bb'}(\mathbf{q},0) = -\frac{1}{N}\sum_{\mathbf{k},\nu,\nu'}\frac{u^a_{\nu\mathbf{k}}(u^b_{\nu\mathbf{k}})^* u^{b'}_{\nu'(\mathbf{k}+\mathbf{q})}(u^{a'}_{\nu'(\mathbf{k}+\mathbf{q})})^*}{E_{\nu'}(\mathbf{k}+\mathbf{q})-E_\nu(\mathbf{k})} \times\left(f(E_{\nu'}(\mathbf{k}+\mathbf{q}))-f(E_\nu(\mathbf{k}))\right)\ , \tag{13}$$

where

$$f(E_\nu(\mathbf{k}))=\frac{1}{e^{\frac{E_\nu(\mathbf{k})-\mu}{T}}+1}$$

denotes the Fermi distribution function.

In Fig. 3 (a)-(c) we show the results for the total bare spin susceptibility $\chi^0(\mathbf{q},0)=\frac{1}{2}\chi^0_{aabb}(\mathbf{q},0)$ where the x^2-y^2 and $3z^2-r^2$ orbitals have been projected out by setting all components of the eigenvectors $u^{x^2-y^2}_\nu(\mathbf{k})$ and $u^{3z^2-r^2}_\nu(\mathbf{k})$ equal to zero. We note that the results do not change significantly if these orbitals are included, since they do not contribute to the Fermi surface.

The bare susceptibility $\chi^0(\mathbf{q})$ is overall rather flat with small peaks at $(0,\pi)$ and $(\pi,0)$ for $y=0$ (Fig. 3 (a)), almost featureless for $y=0.07$ (Fig. 3 (b)), and with a wide region of enhanced fluctuations in the vicinity of the Γ point for $y=0.15$ (Fig. 3 (c)). All these features are displayed in Fig. 4 (a), where we plot the bare spin susceptibilities for different values of y along the high-symmetry path $\Gamma=(0,0)\to X=(\pi,0)\to M=(\pi,\pi)\to\Gamma=(0,0)$. Red, green and blue lines correspond to $y=0.0$, 0.07 and 0.15, respectively. As in Figs.

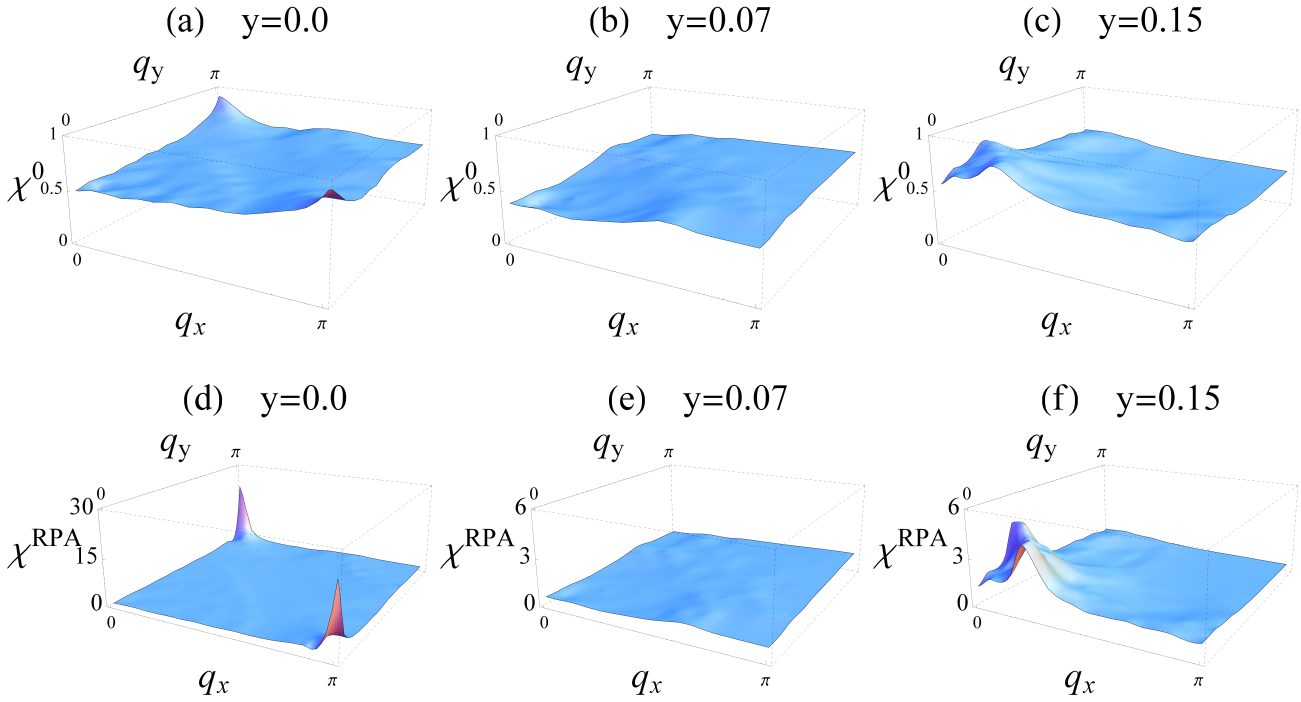

FIG. 3: (Color online) (a)-(c) The bare static spin susceptibility $\chi^0(\mathbf{q},0)$ and (d)-(f) the RPA spin susceptibility $\chi^{\rm RPA}(\mathbf{q},0)$ calculated using the TBM after projecting out the x^2-y^2 and $3z^2-r^2$ orbitals. The concentration of excess Fe is (a) and (d) $y=0.0$; (b) and (e) $y=0.07$; (c) and (f) $y=0.15$. The RPA spin susceptibility is calculated for $U=1.0$ eV and $J_H=U/5$.

3 (a)-(c), we see that for $y=0.0$ the bare susceptibility shows enhanced fluctuations peaked at the $X=(\pi,0)$ point, whereas for $y=0.15$ the magnetic spectral weight is shifted to the vicinity of $\Gamma=(0,0)$ point. For intermediate values of y, the bare susceptibility is basically featureless.

B. RPA susceptibility

The effect of correlations among the itinerant electrons on the spin susceptibility can be taken into account in the framework of the RPA. The RPA spin susceptibility can be obtained using the Dyson equation:[43]

$$\chi^{\rm RPA}_{aa'bb'}(\mathbf{q},\omega) = \chi^0_{aa'bb'}(\mathbf{q},\omega) + \chi^0_{aa'cc'}(\mathbf{q},\omega)\, V_{cc'dd'}\, \chi_{dd'bb'}(\mathbf{q},\omega)\ , \quad (14)$$

where the matrix elements $V_{cc'dd'}$ take into account all electron correlations in the RPA. The interaction parameters which give the strongest contributions are those from the matrix elements $V_{cccc}=U$, $V_{ccdd}=J_H$, $V_{cddc}=J_H$, and $V_{cdcd}=U-2J_H$. All other matrix elements are set to 0. In our calculations we have set $U=1.0$ eV and $J_H=U/5$. Both the Coulomb repulsion and the Hund's coupling are well inside the range of the interaction parameters previously considered in the literature: the lowest estimate of $J_H/U=0.15$ was used in Ref.[28] and the upper limit of $J_H/U=0.25$ was considered in several works, e.g., in Refs.[41,46]. Selecting J_H inside this range ensures that an electron added to an undoped site pays more energy to Coulomb repulsion than it wins from the Hund's rule, i.e., that the onsite interaction energy suppresses charge fluctuations rather than enhancing them.[46]

In Figs. 3 (d)-(f), we present the static RPA spin susceptibility for different values of y. Overall, $\chi^{\rm RPA}(\mathbf{q},0)$ shows a significant enhancement due to interactions – notice, for instance, the different scales used in Figs. 3 (a)-(f). The RPA susceptibility for $y=0.0$ is shown in Fig. 3 (d). The small peaks at the wave vectors $(\pi,0)$ and $(0,\pi)$ observed in the bare susceptibility now display a nearly-diverging behavior. However, similarly to the bare susceptibility, $\chi^{\rm RPA}(\mathbf{q},0)$ for $y=0.0$ does not display significant spin fluctuations near the $(\pm\pi/2,\pm\pi/2)$ points, corresponding to the ordering vectors of the experimentally observed magnetic order.

With increasing y (see Fig. 3 (e) and Fig. 3 (f)), we observe significant changes in the overall structure of the spin susceptibility. As it is particularly seen in Fig. 4 (b), where we show the RPA spin susceptibility along the main symmetry directions, the susceptibility near $(\pi,0)$ and $(0,\pi)$ rapidly decreases with increasing y, and the dominant magnetic response shifts to the vicinities of the Γ point. This is consistent with the loss of nesting features in the Fermi surface. For $y=0.07$ (Fig. 3 (e)), the susceptibility is almost uniform across the whole Brillouin zone. For higher values of y (see Fig. 3 (f)), the susceptibility shows dominant but not diverging behavior

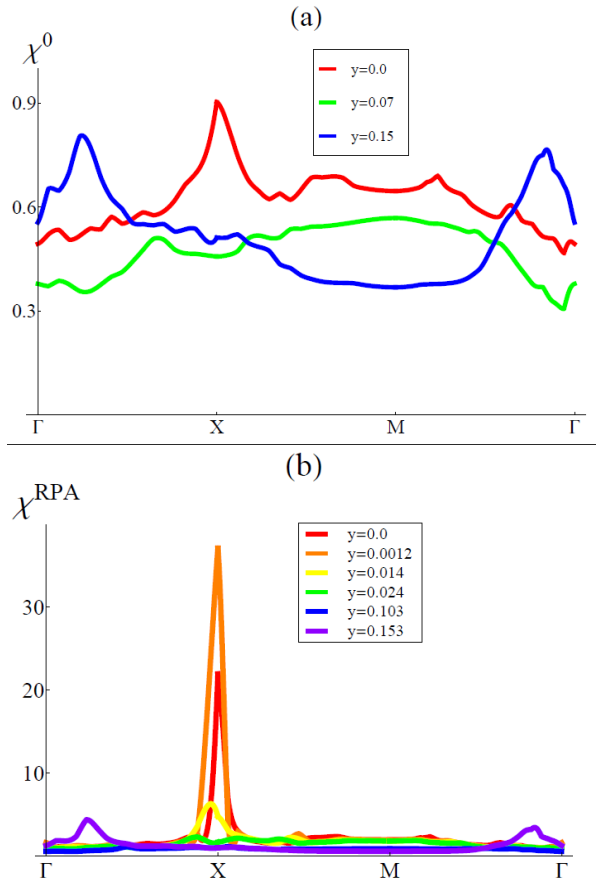

FIG. 4: (Color online) (a) Cut of the bare spin susceptibility along a high-symmetry path. Red, green and blue lines correspond to $y = 0.0$, 0.07 and 0.15, respectively. (b) Cut of the RPA enhanced spin susceptibility along the same high-symmetry path. The legend provides the y values of each line. We use the following notations: $\Gamma = (0,0)$, $X = (\pi, 0)$, and $M = (\pi, \pi)$. The RPA spin susceptibility is calculated for $U = 1.0$ eV and $J_H = U/5$.

in the central part of Brillouin zone close to the Γ point.

V. THE RKKY EXCHANGE INTEGRALS

Equation (9) shows that the RKKY exchange integrals $J_{ij}^{\rm RKKY}$ are proportional to the static magnetic susceptibility of the multi-orbital conduction electrons. Thus, the changes in the spin susceptibility promoted by the increase in the concentration of interstitial Fe discussed in the previous section will lead to changes in $J_{ij}^{\rm RKKY}$ and, according to Eq. (10), to changes in the effective Hamiltonian of the localized spins.

A. Toy model for the RKKY interaction

As shown in Fig. 4 (b), one of the main effects of increasing y on the spin susceptibility is to suppress the nesting-induced peaks at momenta $(\pi, 0)$ and $(0, \pi)$. To shed light on how these changes are translated in changes of the RKKY exchange interactions, we first consider a simple toy model in which the spin susceptibility is given by the phenomenological expression[35]:

$$\chi^{-1}(\mathbf{q}) = \frac{1 + \alpha\left[\cos q_x \cos q_y - \frac{1}{8}\left(\cos 2q_x + \cos 2q_y\right)\right]}{\chi_0\left(1 + \frac{3}{4}\alpha\right)} \quad (15)$$

Here, χ_0 sets the overall scale for magnetic fluctuations and $\alpha < 1$ is a parameter that controls the height and width of the peaks at $(\pi, 0)\,/\,(0, \pi)$. The overall amplitude of the magnetic susceptibility is kept unchanged by the term $\left(1 + \frac{3}{4}\alpha\right)$ in the denominator. In Fig. 5 (a) we plot this phenomenological static magnetic susceptibility along the $X - \Gamma$ direction, $\chi(q_x, 0)$ for $\alpha = 0.2$ (magenta) and $\alpha = 0.6$ (blue), illustrating how the peak at $(\pi, 0)$ decreases with decreasing α. Thus, decreasing α mimics the effect of increasing y in Fig. 4 (b) (at least for small y).

Next we compute the RKKY interactions as a function of α. Taking the Fourier transforms, we obtain:

$$J_1^{\rm RKKY} = -J_H^2 \sum_{\mathbf{q}} \chi(\mathbf{q})\left(\cos q_x + \cos q_y\right) \quad (16)$$

$$J_2^{\rm RKKY} = -J_H^2 \sum_{\mathbf{q}} \chi(\mathbf{q}) \cos q_x \cos q_y \quad (17)$$

$$J_3^{\rm RKKY} = -J_H^2 \sum_{\mathbf{q}} \chi(\mathbf{q})\left(\cos 2q_x + \cos 2q_y\right) \quad (18)$$

A straightforward evaluation gives the results shown in Fig. 5(b). While $J_1^{\rm RKKY} = 0$ for all values of α, we note that $J_2^{\rm RKKY} > 0$ and $J_3^{\rm RKKY} < 0$, with $J_2^{\rm RKKY} \approx \left|J_3^{\rm RKKY}\right|$. As the peak intensity decreases (i.e. as α decreases), the absolute values of $J_2^{\rm RKKY}$ and $J_3^{\rm RKKY}$ decrease strongly.

This behavior can be understood in a straightforward way by noting that only the structure factors of $J_2^{\rm RKKY}$ and $J_3^{\rm RKKY}$ in Eq. (18) match the Fourier components of the magnetic susceptibility in Eq. (15). To make this argument even more transparent, consider an even simpler model for the magnetic susceptibility consisting of a constant background plus peaks at $\mathbf{Q}_X = (\pi, 0)$ and $\mathbf{Q}_Y = (0, \pi)$:

$$\frac{\chi(\mathbf{q})}{\chi_0} = 1 + \alpha\left[\delta(\mathbf{q} - \mathbf{Q}_X) + \delta(\mathbf{q} - \mathbf{Q}_Y)\right] \quad (19)$$

It is straightforward to obtain:

$$\begin{aligned} J_1^{\rm RKKY}/(J_H^2\chi_0) &= -2\alpha\left(\cos\pi + \cos 0\right) = 0 \\ J_2^{\rm RKKY}/(J_H^2\chi_0) &= -2\alpha\left(\cos\pi\cos 0\right) = 4\alpha \\ J_3^{\rm RKKY}/(J_H^2\chi_0) &= -2\alpha\left(\cos 2\pi + \cos 0\right) = -4\alpha \end{aligned}$$

in agreement with Fig. 5 (b). Thus, this toy model shows that peaks at $(\pi, 0)$ and $(0, \pi)$ in the itinerant susceptibility induce local-spin interactions only between second and third neighbors, without affecting the first-neighbors

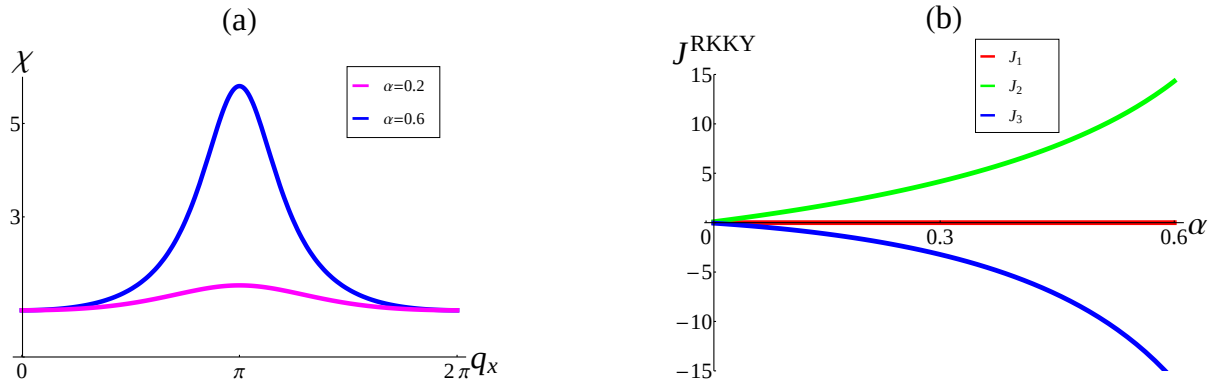

FIG. 5: (a) Static magnetic susceptibility $\chi(q_x, 0)$ of the toy model (15) for $\alpha = 0.2$ (magenta) and $\alpha = 0.6$ (blue). (b) $J^{\rm RKKY}$ (in units of $J_H^2\chi_0$) of the same toy model as function of the $(\pi, 0)\,/\,(0, \pi)$ peak intensity α. $J_1^{\rm RKKY}$, $J_2^{\rm RKKY}$ and $J_3^{\rm RKKY}$ are shown by red, green, and blue lines, respectively.

interaction. The latter is, however, very sensitive to the fluctuations peaked at different wave vectors, as we will see in more realistic calculations in the next subsection, in particular to the fluctuations with small-**q** vectors.

B. RKKY interactions computed within the TBM

We now compute the RKKY interactions numerically using the results for the susceptibility obtained in Sec. IV. For completeness, we compute the RKKY interactions up to the sixth-nearest neighbors for different concentrations of excess interstitial Fe, y. In Fig. 6 (a) we plot $J_1^{\rm RKKY}$, $J_2^{\rm RKKY}$ and $J_3^{\rm RKKY}$ – shown, correspondingly, in red, green and blue solid lines – and $J_4^{\rm RKKY}$, $J_5^{\rm RKKY}$ and $J_6^{\rm RKKY}$ – shown, correspondingly, in brown, orange and purple dashed lines. $J_4^{\rm RKKY} - J_6^{\rm RKKY}$ interactions are small almost for almost all values of y, except $J_5^{\rm RKKY}$ at interstitial concentrations $y < 0.015$. However, as $Fe_{1+y}Te$ crystals have not been yet grown with $y < 0.015$, we will not discuss the possible effects of this term.

For small but physical values of y, the largest interactions are $J_2^{\rm RKKY}$ and $J_3^{\rm RKKY}$, whereas for intermediate and larger values of y, $J_1^{\rm RKKY}$ dominates. Because of this, and since in our bare local model (5) only J_1, J_2, and J_3 have non-zero values, hereafter we neglect the RKKY contributions beyond third-nearest neighbors.

Much of the behavior of the RKKY interactions for small values of y can be understood within the toy model discussed in the previous section. As expected, we obtain large antiferromagnetic $J_2^{\rm RKKY}$ and ferromagnetic $J_3^{\rm RKKY}$ interactions in the regime where the susceptibility $\chi^{\rm RPA}(\mathbf{q}, 0)$ has strong peaks near the $(\pi, 0)$ and $(0, \pi)$ points ($y \lesssim 0.025$, see Fig. 4 (b)). As these peaks are suppressed, the absolute values of both interaction parameters are reduced, in agreement with decreasing α in Fig. 5 (b). At the same time, the small antiferromagnetic $J_1^{\rm RKKY}$ interaction remains nearly unchanged, reflecting the fact that it is unaffected by the fluctuations near $(\pi, 0)$ and $(0, \pi)$. In contrast, fluctuations in broader regions of the Brillouin zone, such as in the vicinities of the M and the Γ points, yield the leading contributions to the $J_1^{\rm RKKY}$ interaction.

By increasing the concentration of interstitial Fe atoms beyond $y \approx 0.025$, the $J_1^{\rm RKKY}$ interaction becomes the dominant one, as the large peaks of the itinerant susceptibility $\chi^{\rm RPA}(\mathbf{q}, 0)$ near $(\pi, 0)$ and $(0, \pi)$ quickly disappear, rendering $J_2^{\rm RKKY}$ and $J_3^{\rm RKKY}$ small. However, for $y \gtrsim 0.05$, the antiferromagnetic $J_1^{\rm RKKY}$ interaction starts being suppressed, and eventually changes sign and becomes ferromagnetic for $y \gtrsim 0.1$. Comparison to the behavior of the RPA susceptibility in Fig. 4 (b) reveals that this change can be attributed to the reduction of the broad fluctuations present around the M point, followed by the subsequent enhancement of fluctuations near the Γ point. Indeed, according to the form factor of $J_1^{\rm RKKY}$ in Eq. (18), fluctuations around $M = (\pi, \pi)$ yield an antiferromagnetic $J_1^{\rm RKKY}$, whereas fluctuations around $\Gamma = (0, 0)$ yield a ferromagnetic $J_1^{\rm RKKY}$.

C. Derivation of the effective couplings

Having calculated $J_{ij}^{\rm RKKY}$ as function of the Fe excess concentration, it is now straightforward to compute the y-dependent effective couplings $J_{ij}^{\rm eff}$ between the localized moments in Eq. (10), whose solution determines the magnetic ground state. To this end, we first need to establish the bare Heisenberg exchange couplings J_{ij}, which do not change with increasing Fe excess. The values of the effective couplings $J_{ij}^{\rm eff}$ at $y \simeq 0$ were computed via first-principles electronic structure calculations by Ma *et al.*[14] Up to the third neighbors, these values normalized on the value of spin S are equal to $J_1^{\rm eff}$ =2.1 meV/S^2, $J_2^{\rm eff}$ =15.8 meV/S^2, $J_3^{\rm eff}$ =10.1 meV/S^2. Because even for $y \simeq 0$, $Fe_{1+y}Te$ has both itinerant and localized electrons, these effective couplings contain both the $J_{ij}^{\rm RKKY}$

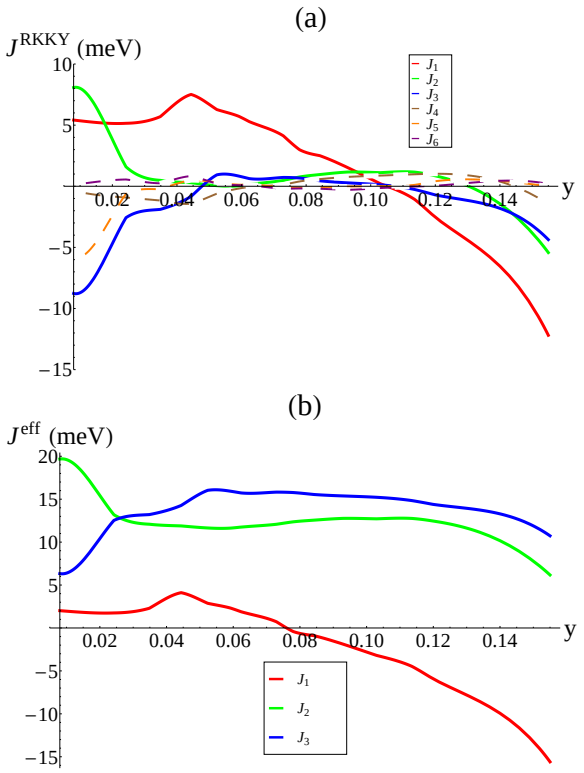

FIG. 6: (Color online) (a) The evolution of $J_1^{\rm RKKY}$ (red solid line), $J_2^{\rm RKKY}$ (green solid line), $J_3^{\rm RKKY}$ (blue solid line) with increasing concentration of excess of interstitial Fe atoms y. The other neighbor interactions are $J_4^{\rm RKKY}$ (brown dashed line), $J_5^{\rm RKKY}$ (orange dashed line), $J_6^{\rm RKKY}$ (purple dashed line). (b) The evolution of the effective exchange couplings $J_{ij}^{\rm eff}$, where $J_1^{\rm eff} = -3.4 + J_1^{\rm RKKY}(y)$ (red line), $J_2^{\rm eff} = 11.6 + J_2^{\rm RKKY}(y)$ (green line), and $J_3^{\rm eff} = 15.1 + J_3^{\rm RKKY}(y)$ (blue line). All interactions are given in meV/S^2.

interactions and the bare Heisenberg exchange couplings J_{ij}. In order to decompose these contributions, we simply subtract the RKKY interactions computed by us at $y = 0$ from the values of the super-exchange interactions derived by Ma *et al.*[14] This procedure yields the bare Heisenberg exchange couplings $J_1 = -3.4$ meV/S^2, $J_2 = 11.6$ meV/S^2, and $J_3 = 15.1$ meV/S^2.

In Fig. 6 (b), we plot $J_{ij}^{\rm eff}(y) = J_{ij} + J_{ij}^{\rm RKKY}(y)$ as a function of y. We note that the effective couplings $J_2^{\rm eff}$ and $J_3^{\rm eff}$ remain antiferromagnetic for all y, while $J_1^{\rm eff}$ changes sign at $y = 0.075$. As we will show in the next section, this change in $J_1^{\rm eff}$ is the driving force behind the change in the magnetic order that happens in $Fe_{1+y}Te$ above a critical concentration of Fe excess.

VI. CLASSICAL PHASE DIAGRAM

With the y-dependent exchange constants shown in Fig. 6 (b), we now proceed to the solution of the effective super-exchange model (10). We compute the classical phase diagram by numerical minimization of its classical energy with the constraint that all spins have unit length. Our findings are summarized in the classical phase diagram presented in Fig. 7. To look for a wide variety of states, we introduce four sublattices, labeled as 0, 1, 2, and 3 (see Fig. 8) and perform full minimization of the classical energy. To each sublattice we associate a local frame given by angles $\varphi_0, \varphi_1, \varphi_2, \varphi_3$. We define the global reference frame by setting $\varphi_0 = 0$. In addition, we consider only spin configurations which can be characterized by a single-$\mathbf{q}$ spiral, such that after a translation from site to site in the same sublattice, the magnetic moment rotates by an angle $\theta = \mathbf{q}\cdot\mathbf{r}$, where $\mathbf{r} = 2\,m\,a_x + 2\,n\,a_y$, m and n are integers, $\mathbf{a} = (a_x, a_y)$ is the lattice vector. Then, the general expression for the on-site magnetization is given by

$$\bar{\mathbf{S}}_\mu(\mathbf{r}) = \hat{\mathbf{x}}\,\sin(\mathbf{q}\cdot\mathbf{r} + \varphi_\mu) + \hat{\mathbf{y}}\,\cos(\mathbf{q}\cdot\mathbf{r} + \varphi_\mu), \quad (20)$$

where $\mu = 0, 1, 2, 3$ is the sublattice index. Substituting $\bar{\mathbf{S}}_\mu(\mathbf{r})$ into Eq.(10) yields the classical energy $E_{\rm cl} = E(\{\varphi_\mu\}, \mathbf{q})$. The explicit expression for the classical energy is rather cumbersome and, for convenience, is given in Appendix B. We minimize E_{cl} numerically and for each set of parameters $J_{ij}^{\rm eff}$ and K_{ij} we find the classical ground state characterized by φ_1, φ_2, φ_3, q_x, and q_y. In our computation we fix the second-neighbor biquadratic exchange to be equal to $K_2 = 3.0$ meV/S^2, but our results do not depend strongly on this value. We vary therefore two parameters of the model: the nearest-neighbor biquadratic exchange K_1 and the excess iron concentration y, which affects indirectly the effective exchange couplings $J_{ij}^{\rm eff}$ via the RKKY interaction.

In Figs. 8 (a)-(c), we draw the real-space spin configurations presented in the phase diagram of Fig. 7. Among all possible states, in the parameter space presented in the phase diagram, only three states are realized: the stripe phase characterized by $\varphi_1 = 0$, $\varphi_2 = \pi$, $\varphi_3 = \pi$, $q_x = 0$, $q_y = 0$ shown in Fig. 8 (a), the double stripe phase characterized by $\varphi_1 = 0$, $\varphi_2 = 0$, $\varphi_3 = \pi$, $q_x = \pi/2$, $q_y = \pi/2$ shown in Fig. 8 (b) and the incommensurate spiral (labeled as IC) state shown in Fig. 8 (c) characterized by $\varphi_1 = \pi/2 - \delta$, $\varphi_2 = \pi - 2\delta$, $\varphi_3 = \pi/2 - \delta$, $q_x = \pi/2 - \delta$, $q_y = \pi/2 - \delta$. Note that in Fig. 8 (c) we show the IC state with an exaggerated canting angle. To clarify the structure of these different orderings, we also take the Fourier transforms of the ground state spin configuration obtained by the minimization and then compute the corresponding spin structure factor. As expected, the structure factor exhibits peaks at the following ordering wave-vectors: $\mathbf{Q} = (0, \pi)$ for the stripe phase, $\mathbf{Q} = (\pi/2, \pi/2)$ for the bicollinear double-stripe phase, and $\mathbf{Q} = (\pi/2 - \delta, \pi/2 - \delta)$ for the IC phase.

The structure of the phase diagram (see Fig. 7) can be summarized as follows. For small values of y, there is a thin strip of the single-stripe phase. This phase is stabilized by a strong $J_2^{\rm eff}$ coupling (see Fig. 6 (b)) and quickly disappears because $J_2^{\rm eff}$ decreases rapidly with increasing y. We believe that the stripe phase has not

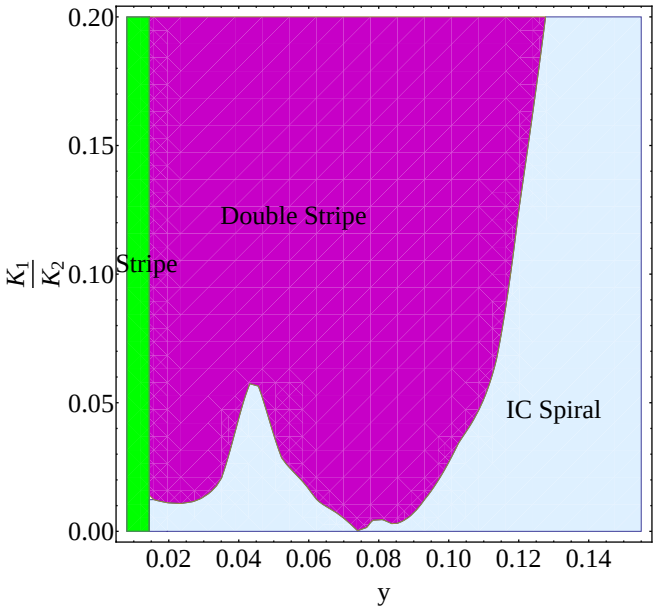

FIG. 7: (Color online) Magnetic phase diagram of the effective low-energy model (10) as a function of Fe excess y and the ratio between the first- and second-neighbor biquadratic exchanges, $\frac{K_1}{K_2}$, computed with (in meV/S^2 units) $J_1^{\rm eff}(y) = -3.4 + J_1^{\rm RKKY}(y)$, $J_2^{\rm eff}(y) = 11.6 + J_2^{\rm RKKY}(y)$, $J_3^{\rm eff}(y) = 15.1 + J_3^{\rm RKKY}(y)$. The RKKY interactions $J_{ij}^{\rm RKKY}$ are shown in Fig. V B. We set $K_2 = 3$.

been observed in $Fe_{1+y}Te$ because all known compounds belonging to this family are, actually, nonstoichiometric and have a small amount of interstitial Fe significantly larger than the boundary value of $y = 0.014$ below which the stripe phase is stable.

The central region in the phase diagram ($y > 0.014$) is occupied by the bicollinear double-stripe state. This is the state which is experimentally observed in the $Fe_{1+y}Te$ compound with a low level of excess Fe. The stability of this phase over a wide range of parameters is explained by the smallness of the effective nearest-neighbor coupling $J_1^{\rm eff}$ and relatively strong strength of the third-neighbor coupling $J_3^{\rm eff}$. The biquadratic couplings K_{ij} among which the dominating role is played by K_2 and $K_{\rm diag} = -K_2$ (see Appendix A), also play an important role in stabilizing this state: except in the region near $y = 0.075$, a finite value of the nearest-neighbor biquadratic coupling K_1 is necessary to stabilize the double stripe phase over the incommensurate spiral state. The region near $y = 0.075$ is rather peculiar, as there the effective nearest neighbor coupling $J_1^{\rm eff}$ is equal to zero or is very small compared with the other interactions, making the bicollinear double stripe state the most stable one even in the absence of the biquadratic exchange. The rest of the phase diagram is occupied by an IC phase (see, Fig. 8 (c)), which is the (q, q) spiral state experimentally observed for sufficiently large y.

In the experiment performed in Ref.[11], the phase transition from the bicollinear double stripe to the IC phase was observed approximately for $y \approx 0.11$. This is consistent with our phase diagram presented in Fig. 7 if one takes $\frac{K_1}{K_2} \simeq 0.1$, which seems to be a realistic ratio, since the magneto-elastic coupling favors the biquadratic exchange between second neighbors (see Appendix A for more details). We emphasize that, because our model contains assumptions about the bare values of J_{ij} and the amount of electrons introduced by each excess Fe, the precise value of y for which the transition takes place is beyond our scope. Yet, the general tendency of a double-stripe to IC transition for increasing charge doping encoded in the phase diagram of Fig. 7 is robust and consistent with the experimental observations.

VII. CONCLUSIONS

In summary, we have studied the evolution of the magnetic order in $Fe_{1+y}Te$ as function of y. Starting with a model containing both localized spins and itinerant electrons, we derived an effective superexchange Hamiltonian to describe the magnetic properties of $Fe_{1+y}Te$ which contains both the long-range RKKY-type spin-spin interaction mediated by the itinerant electrons and the biquadratic interactions due to magneto-elastic effects. Thus, y-dependent exchange interactions naturally arise in our model due to changes in the low-energy itinerant electronic states promoted by charge doping.

After calculating the classical phase diagram of the y-dependent effective superexchange model, we showed that $Fe_{1+y}Te$ has a general tendency for a double-stripe to incommensurate-spiral transition with increasing excess iron concentration. In particular, for small y, the magnetic order is a double-stripe state, arising due to the presence of a significant antiferromagnetic $J_3^{\rm eff}$ coupling, which has mostly localized origin. Beyond a certain critical value of y, the incommensurate spiral state becomes the most stable. This transition is driven not only by the suppression of the antiferromagnetic exchanges $J_3^{\rm eff}$ and $J_2^{\rm eff}$, but also by the enhancement (in absolute value) and sign change of the nearest-neighbor $J_1^{\rm eff}$ interaction, which changes from antiferromagnetic to ferromagnetic with increasing y. These changes are caused by the y-dependent RKKY part of the interaction, and ultimately can be attributed to the suppression of the $(\pi, 0)$ / $(0, \pi)$ peaks in the itinerant spin-susceptibility and the transfer of magnetic spectral weight from the vicinities of (π, π) to the vicinities of $(0, 0)$. These changes, in turn, are a direct consequence of the changes in the Fermi surface of the itinerant electrons caused by the charge doping introduced by the excess Fe. Experimental data showing the sign of $J_1^{\rm eff}$ to be dependent on the interstitial Fe concentration would be a strong validation of our model. The physics of $Fe_{1+y}Te$ discussed here bares many similarities with extensively studied double-exchange magnets, and in particular with manganites, whose effective coupling constants were shown to be significantly modified by charge doping.[47–49] In both cases, the interplay

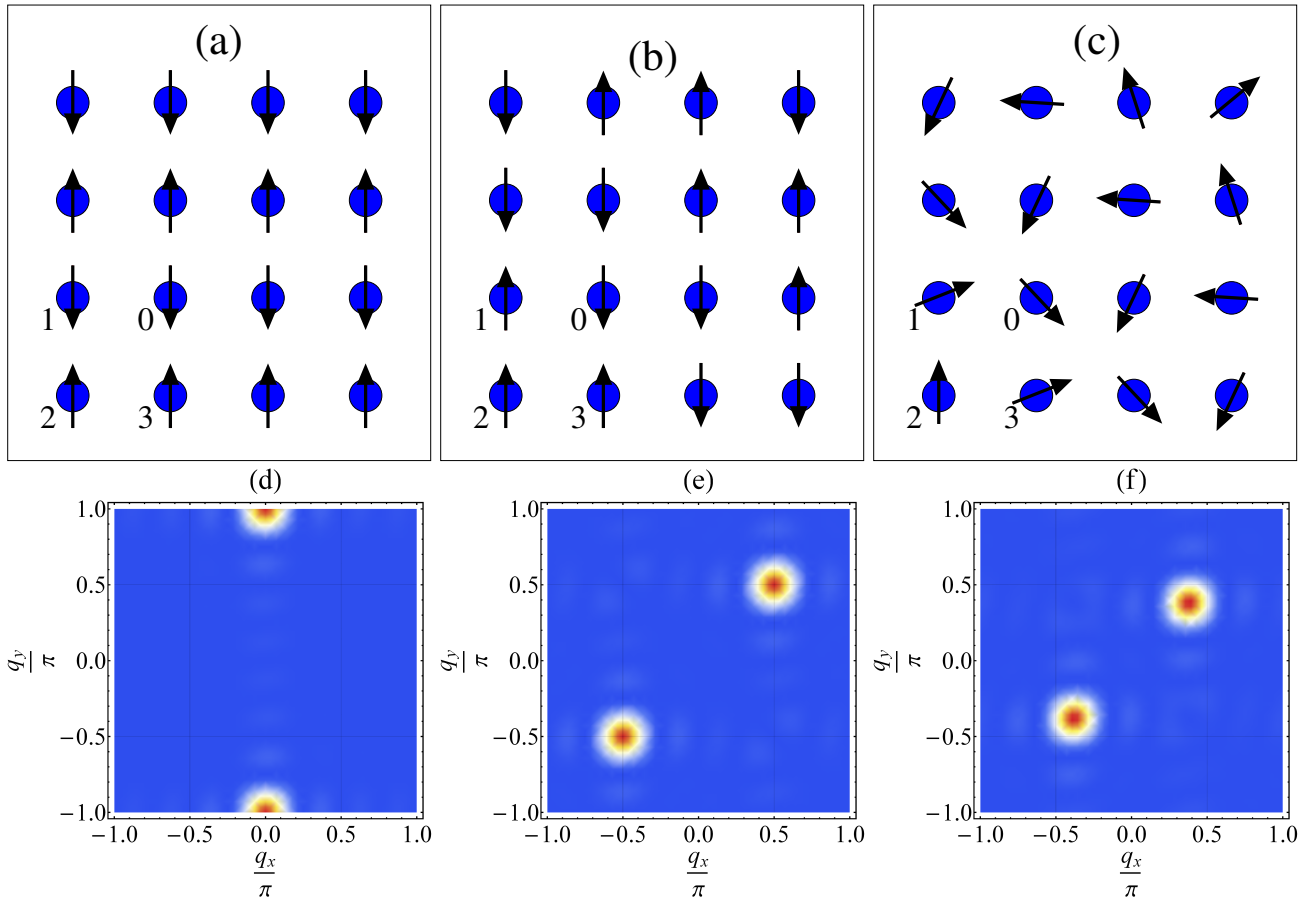

FIG. 8: (Color online) Schematic representations of the spin configurations in the ground state obtained by the minimization of the classical energy with respect to $\varphi_1, \varphi_2, \varphi_3, q_x$, and q_y: (a) $\varphi_1 = 0, \varphi_2 = \pi, \varphi_3 = \pi, q_x = 0, q_y = 0$ gives the single-stripe phase, (b) $\varphi_1 = 0, \varphi_2 = 0, \varphi_3 = \pi, q_x = \pi/2, q_y = \pi/2$ gives the double-stripe phase, (c) $\varphi_1 = \pi/2 - \delta, \varphi_2 = \pi - 2\delta, \varphi_3 = \pi/2 - \delta, q_x = \pi/2 - \delta, q_y = \pi/2 - \delta$ gives the incommensurate spiral phase. (d),(e) The structure factors computed for the magnetic orders displayed in (a)-(c), respectively. Bright spots correspond to the sharp peaks that appear at the corresponding ordering wavevectors.

between local moments and itinerant electrons leads to a rich behavior and to the appearance of new ground states in the classical phase diagram.

Acknowledgement. We acknowledge useful conversations with A. Chubukov, I. Eremin, M. Gingras, M. Imada, D.H. Lee, I. Mazin, I. Paul, S. and U. Roessler and I.Zaliznyak. We especially thank F. Wang and Z.-Y. Lu for providing us with the unfolded five orbital tight-binding model, which we use in this work. N.B.P. and S. D. are supported by NSF grant DMR-1255544. N.B.P. and R. M. F. acknowledge the hospitality of the Aspen Center for Physics, and also NSF grant No.1066293 supporting the center.

Appendix A: Derivation of biquadratic exchange couplings

There are several microscopic mechanisms which lead to non-Heisenberg exchange couplings such as, e.g., biquadratic and ring exchanges. Among all of them, one of the most effective ways to induce a fairly strong non-Heisenberg exchange is through the coupling to the lattice via the magneto-elastic effect. In the pnictides and chalcogenides, this key role played by the magnetoelastic coupling was extensively discussed, see Refs.[35–37].

Here, we present a brief discussion of the possible magnetoelastic origin of the first- and the second-neighbor biquadratic exchange interactions K_1 and K_2 in $Fe_{1+y}Te$. Motivated by the experimentally measured lattice distortions, which are small, we assume a linear regime in which exchange interactions and elastic energies depend only on the distance between lattice sites. As the magneto-elastic Hamiltonian involves more than one normal mode of a square lattice, it is convenient to follow the notation of Ref.[36] and describe the lattice distortions by the strain tensor separated in uniform and non-uniform parts:

$$u_{ij}(\mathbf{r}) = u_{ij} + \frac{\imath}{2}\sum_{q\neq 0}(q_i u_j(\mathbf{q}) + q_i u_j(\mathbf{q}))e^{\imath\mathbf{q}\cdot\mathbf{r}}. \quad \text{(A1)}$$

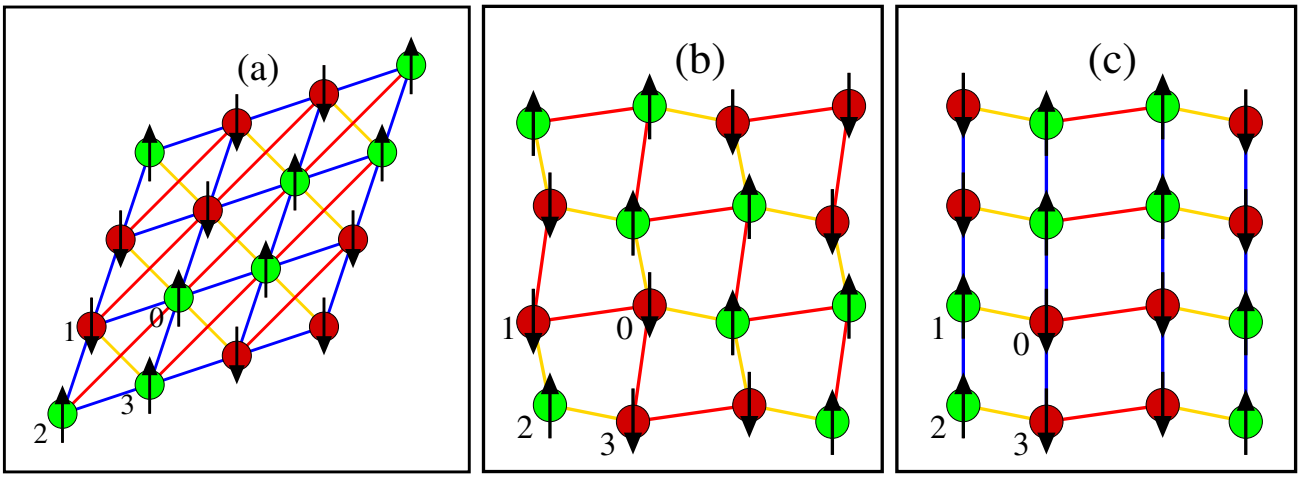

FIG. 9: Most relevant elastic modes in $Fe_{1+y}Te$. (a) The uniform monoclinic mode, u_{xy}. (b) The non-uniform mode corresponding to $u_5^x = u_5^y$. (c) The non-uniform mode corresponding to the u_6 distortion. The mode corresponding to the u_7 distortion would display the same configuration but rotated by 90°. We use the following convention: red bonds are lengthened with respect to the tetragonal lattice, yellow bonds are shortened, blue bonds remain of the same length. Green (red) sites have spins ferromagnetically (antiferromagnetically) aligned with each other.

The most relevant $\mathbf{q} = 0$ lattice modulation in $Fe_{1+y}Te$ is the monoclinic distortion, given by $u_{xy} \equiv \partial_y u_x + \partial_x u_y$, and illustrated in Fig. 9(a). It corresponds to a distortion of the square in a rhombus with a short and a long diagonal. The most relevant non-uniform lattice modulations are those with modulation vectors $\mathbf{q}_5 = (\pi, \pi)$, $\mathbf{q}_6 = (\pi, 0)$ and $\mathbf{q}_7 = (0, \pi)$. To make the notations simpler, we denote $u(\mathbf{q}_5) \equiv u_5$, $u(\mathbf{q}_6) \equiv u_6$ and $u(\mathbf{q}_7) \equiv u_7$. The real space patterns of the first two are shown in Figs. 9(b)-(c). The non-uniform mode corresponding to u_5 generates a distortion with ladders along the diagonal of short and long nearest-neighbor bonds. On the other hand, the non-uniform mode corresponding to the u_6 (u_7) distortion has bonds that alternate between short and long in the x-direction (y-direction).

Using this notation, the dominant magneto-elastic term is given by[36]

$$\begin{aligned} H_{\rm ME} &= g_1(\mathbf{S}_1\cdot\mathbf{S}_3 - \mathbf{S}_0\cdot\mathbf{S}_2)u_{xy} \\ &+ g_2\left[(\mathbf{S}_2\cdot\mathbf{S}_3 - \mathbf{S}_0\cdot\mathbf{S}_1)u_5^x + (\mathbf{S}_1\cdot\mathbf{S}_2 - \mathbf{S}_0\cdot\mathbf{S}_3)u_5^y\right] \\ &+ g_3\left[(\mathbf{S}_2\cdot\mathbf{S}_3 + \mathbf{S}_0\cdot\mathbf{S}_1)u_6^x + (\mathbf{S}_1\cdot\mathbf{S}_2 + \mathbf{S}_0\cdot\mathbf{S}_3)u_7^y\right]. \end{aligned} \tag{A2}$$

where g_i are the magneto-elastic couplings. The spins $\mathbf{S}_i$ with $i = 0, ..., 3$ correspond to the four spins in the sublattice shown in Fig. 8a of the main text.

Because the elastic modes are assumed to be non-critical, the elastic energy acquires a harmonic form:

$$H_{\rm elast} = \frac{c_{66}}{2}u_{xy}^2 + \frac{\Omega_1}{2}u_5^2 + \frac{\Omega_2}{2}(u_6^2 + u_7^2)\ , \tag{A3}$$

where the constants c_{66}, Ω_1, and Ω_2 represent the elastic stiffness of the different lattice distortions described by u_{xy}, u_5, and u_6/u_7, respectively. The equilibrium lattice distortions u_{xy}, u_5, u_6, and u_7 are found by minimizing the energy:

$$\begin{aligned} u_{xy} &= -\frac{g_1}{c_{66}}(\mathbf{S}_1\cdot\mathbf{S}_3 - \mathbf{S}_0\cdot\mathbf{S}_2) \\ u_5^x &= -\frac{g_2}{\Omega_1}(\mathbf{S}_2\cdot\mathbf{S}_3 - \mathbf{S}_0\cdot\mathbf{S}_1) \\ u_5^y &= -\frac{g_2}{\Omega_1}(\mathbf{S}_1\cdot\mathbf{S}_2 - \mathbf{S}_0\cdot\mathbf{S}_3) \\ u_6 &= -\frac{g_3}{\Omega_2}(\mathbf{S}_2\cdot\mathbf{S}_3 + \mathbf{S}_0\cdot\mathbf{S}_1) \\ u_7 &= -\frac{g_3}{\Omega_2}(\mathbf{S}_1\cdot\mathbf{S}_2 + \mathbf{S}_0\cdot\mathbf{S}_3). \end{aligned} \tag{A4}$$

Integrating out the lattice distortions, we obtain the following biquadratic Hamiltonian:

$$\begin{aligned} H_{\rm bi} &= -\frac{g_1^2}{2c_{66}}(\mathbf{S}_1\cdot\mathbf{S}_3 - \mathbf{S}_0\cdot\mathbf{S}_2)^2 \\ &- \frac{g_2^2}{2\mathbf{\Omega}_1}[(\mathbf{S}_2\cdot\mathbf{S}_3 - \mathbf{S}_0\cdot\mathbf{S}_1)^2 + (\mathbf{S}_1\cdot\mathbf{S}_2 - \mathbf{S}_0\cdot\mathbf{S}_3)^2] \\ &- \frac{g_3^2}{2\mathbf{\Omega}_2}[(\mathbf{S}_2\cdot\mathbf{S}_3 + \mathbf{S}_0\cdot\mathbf{S}_1)^2 + (\mathbf{S}_1\cdot\mathbf{S}_2 + \mathbf{S}_0\cdot\mathbf{S}_3)^2]. \end{aligned} \tag{A5}$$

Here it is convenient to rewrite this expression explicitly in terms of the first- and second-neighbor biquadratic interactions K_1 and K_2, as well as of the ring exchange interactions $K_\square$ and $K_{\rm diag}$:

$$
\begin{aligned}
H_{\rm bi} = & -\left(\frac{g_2^2}{2\mathbf{\Omega}_1}+\frac{g_3^2}{2\mathbf{\Omega}_2}\right)\left[(\mathbf{S}_2\cdot\mathbf{S}_3)^2+(\mathbf{S}_0\cdot\mathbf{S}_1)^2+(\mathbf{S}_1\cdot\mathbf{S}_2)^2+(\mathbf{S}_0\cdot\mathbf{S}_3)^2\right]-\frac{g_1^2}{2c_{66}}\left[(\mathbf{S}_1\cdot\mathbf{S}_3)^2+(\mathbf{S}_0\cdot\mathbf{S}_2)^2\right] \quad \text{(A6)}\\
& +\left(\frac{g_2^2}{\mathbf{\Omega}_1}-\frac{g_3^2}{\mathbf{\Omega}_2}\right)\left[(\mathbf{S}_2\cdot\mathbf{S}_3)(\mathbf{S}_0\cdot\mathbf{S}_1)+(\mathbf{S}_1\cdot\mathbf{S}_2)(\mathbf{S}_0\cdot\mathbf{S}_3)\right]+\frac{g_1^2}{c_{66}}(\mathbf{S}_1\cdot\mathbf{S}_3)(\mathbf{S}_0\cdot\mathbf{S}_2)\\
= & -K_1\sum_{\langle ij\rangle}(\mathbf{S}_i\cdot\mathbf{S}_j)^2-K_2\sum_{\langle\langle ij\rangle\rangle}(\mathbf{S}_i\cdot\mathbf{S}_j)^2-K_\square\sum_{\square}(\mathbf{S}_i\cdot\mathbf{S}_j)(\mathbf{S}_k\cdot\mathbf{S}_l)-K_{\rm diag}\sum_{\langle\langle ij\rangle\rangle}(\mathbf{S}_1\cdot\mathbf{S}_3)(\mathbf{S}_0\cdot\mathbf{S}_2)\ ,
\end{aligned}
$$

where

$$
\begin{aligned}
K_1 &= \frac{g_2^2}{\Omega_1}+\frac{g_3^2}{\Omega_2}\\
K_2 &= \frac{g_1^2}{c_{66}}\\
K_\square &= -\frac{g_2^2}{\Omega_1}+\frac{g_3^2}{\Omega_2}\\
K_{\rm diag} &= -\frac{g_1^2}{c_{66}}
\end{aligned}
$$

Because we expect the non-uniform strains u_5, u_6, and u_7 to have a stronger stiffness than the stiffness of the monoclinic distortion u_{xy}, in our calculations we neglected the ring exchange term $K_\square$ and assumed that $K_1 \ll K_2$. Furthermore, we used the fact that $K_{\rm diag} = -K_2$.

Appendix B: Classical energy

Here we present the expression for the classical energy of the local-spin model of Eq. (10), as function of the local angles φ_i and the ordering vector (q_x, q_y):

$$
\begin{aligned}
E_{cl} = & \frac{S^2}{4}\Big[J_1\Big(\cos\varphi_1+\cos(\varphi_1+2q_x)+\cos(\varphi_3-\varphi_2)+\cos(\varphi_3-(\varphi_2+2q_x))+\cos\varphi_3+\cos(\varphi_3+2q_y)\\
& +\cos(\varphi_1-\varphi_2)+\cos(\varphi_1-(\varphi_2+2q_y))\Big)+J_2\Big(\cos\varphi_2+\cos(\varphi_2+2q_x+2q_y)+\cos(\varphi_1-(\varphi_3+2q_y))\\
& +\cos(\varphi_1+2q_x-\varphi_3)+\cos(\varphi_2+2q_y)+\cos(\varphi_1-\varphi_3)+\cos(\varphi_2+2q_x)+\cos((\varphi_1+2q_x)-(\varphi_3+2q_y))\Big)\\
& +4J_3\Big(\cos 2q_x+\cos 2q_y\Big)+K_1S^2\Big(\cos^2\varphi_1+\cos^2(\varphi_1+2q_x)+\cos^2(\varphi_3-\varphi_2)+\cos^2(\varphi_3-(\varphi_2+2q_x))\\
& +\cos^2\varphi_3+\cos^2(\varphi_3+2q_y)+\cos^2(\varphi_1-\varphi_2)+\cos^2(\varphi_1-(\varphi_2+2q_y))\Big)+K_2S^2\Big(\cos^2\varphi_2+\cos^2(\varphi_2+2q_x+2q_y)\\
& +\cos^2(\varphi_1-(\varphi_3+2q_y))+\cos^2(\varphi_1+2q_x-\varphi_3)+\cos^2(\varphi_2+2q_y)+\cos^2(\varphi_1-\varphi_3)+\cos^2(\varphi_2+2q_x)\\
& +\cos^2((\varphi_1+2q_x)-(\varphi_3+2q_y))+\cos\varphi_2\cos(\varphi_1-\varphi_3)+\cos(\varphi_2+2q_x)\cos(\varphi_1+2q_x-\varphi_3)\\
& +\cos(\varphi_2+2q_y)\cos(\varphi_1-\varphi_3-2q_y)+\cos(\varphi_2+2q_x+2q_y)\cos(\varphi_1+2q_x-\varphi_3-2q_y)\Big)\Big]\ .
\end{aligned}
$$

[1] W. Bao, Y. Qiu, Q. Huang, M. A. Green, P. Zajdel, M. R. Fitzsimmons, M. Zhernenkov, S. Chang, M. Fang, B. Qian, E. K. Vehstedt, J. Yang, H. M. Pham, L. Spinu, and Z. Q.Mao, Phys. Rev. Lett. **102**, 247001 (2009).

[2] Y. Xia, D. Qian, L. Wray, D. Hsieh, G. F. Chen, J. L. Luo, N. L. Wang, and M. Z. Hasan, Phys. Rev. Lett. **103**, 037002 (2009).

[3] T.J. Liu et al., Nature Mater. 9, 718 (2010).

[4] O. J. Lipscombe, G. F. Chen, C. Fang, T. G. Perring, D. L. Abernathy, A. D. Christianson, T. Egami, N. Wang, J-P Hu, and P. Dai, Phys. Rev. Lett. **106**, 057004 (2011).

[5] E. E. Rodriguez, C. Stock, P. Zajdel, K. L. Krycka, C. F. Majkrzak, P. Zavalij, and M. A. Green, Phys. Rev. B **84**, 064403 (2011).

[6] Chris Stock, Efrain E. Rodriguez, Mark A. Green, Peter Zavalij, and Jose A. Rodriguez-Rivera, Phys. Rev. B **84**, 045124 (2011).

[7] I. A. Zaliznyak, Z. J. Xu, J. S. Wen, J. M. Tranquada, G. D. Gu, V. Solovyov, V. N. Glazkov, A. I. Zheludev, V. O. Garlea, and M. B. Stone, Phys. Rev. B **85**, 085105 (2012).

[8] Yoshikazu Mizuguchi, Kentaro Hamada, Kazuki Goto, Hiroshi Takatsu, Hiroaki Kadowaki, and Osuke Miura, Solid

State Communications **152**, 1047 (2012).
[9] S. Roessler, D. Cherian, W. Lorenz, M. Doerr, C. Koz, C. Curfs, Yu. Prots, U. K. Roessler, U. Schwarz, S. Elizabeth, and S. Wirth, Phys. Rev. B **84**, 174506 (2011).
[10] C. Koz, S. Roessler, A. A. Tsirlin, D. Kasinathan, C. Boernert, M. Hanfland, H. Rosner, S. Wirth, and U. Schwarz, Phys. Rev. B **86**, 094505 (2012).
[11] Cevriye Koz, Sahana Roessler, Alexander A. Tsirlin, Steffen Wirth, and Ulrich Schwarz, Phys. Rev. B **88**, 094509 (2013).
[12] D. Parshall, G. Chen, L. Pintschovius, D. Lamago, Th. Wolf, L. Radzihovsky, and D. Reznik, Phys. Rev. B **85**, 140515 (2012) .
[13] E. E. Rodriguez, D. A. Sokolov, C. Stock, M. A. Green, O. Sobolev, Jose A. Rodriguez-Rivera, H. Cao, and A. Daoud-Aladine, Phys. Rev. B **88**, 165110 (2013).
[14] F. Ma, W. Ji, J. Hu, Z. Lu, and T. Xiang, Phys. Rev. Lett. **102**, 177003 (2009).
[15] Chen Fang, B. Andrei Bernevig, Jiangping Hu, Eur. Phys. Lett. **86**, 67005 (2009).
[16] Samuel Ducatman, Natalia B. Perkins, and Andrey Chubukov Phys. Rev. Lett. **109**, 157206 (2012).
[17] G. Chen, S. Choi, L. Radzihovsky, Phys. Rev. B **88**, 165117 (2013).
[18] Jiangping Hu, Bao Xu, Wuming Liu, Ningning Hao, and Yupeng Wang, Phys. Rev. B **85**, 144403 (2012).
[19] Z. P. Yin, K. Haule, G. Kotliar, Nature Mater. **10**, 932 (2011).
[20] I. I. Mazin and M. D. Johannes, Nat. Phys. **5**, 141 (2009).
[21] F. Kruger, S. Kumar, J. Zaanen, J. van den Brink, Phys. Rev. B **79**, 054504 (2009).
[22] Wei-Guo Yin, Chi-Cheng Lee, and Wei Ku Phys. Rev. Lett. **105**, 107004 (2010).
[23] Weicheng Lv, Frank Kruger, and Philip Phillips, Phys. Rev. B **82**, 045125 (2010).
[24] Shuhua Liang, Gonzalo Alvarez, Cengiz Sen, Adriana Moreo, Elbio Dagotto, Phys. Rev. Lett. **109**, 047001 (2012).
[25] Pengcheng Dai, Jiangping Hu, and Elbio Dagotto, Nat. Phys. **8**, 709 (2012).
[26] Motoaki Hirayama, Takashi Miyake, and Masatoshi Imada, Phys. Rev. B **87**, 195144 (2013).
[27] K. Haule and G. Kotliar, New J. Phys. **11**, 025021 (2009).
[28] Nicola Lanata, Hugo U. R. Strand, Gianluca Giovannetti, Bo Hellsing, Luca de Medici, and Massimo Capone, Phys. Rev. B **87**, 045122 (2013).
[29] E. Bascones, B. Valenzuela, M. J. Calderon, Phys. Rev. B **86**, 174508 (2012).
[30] Alireza Akbari, Ilya Eremin, Peter Thalmeier, Phys. Rev. B **84**, 134513 (2011).
[31] Alireza Akbari, Peter Thalmeier, and Ilya Eremin, New J. Phys. **15**, 033034 (2013).
[32] Maria N. Gastiasoro and Brian M. Andersen, arXiv:1403.3324.
[33] A. L. Wysocki, K. D. Belashchenko, and V. P. Antropov, Nat. Phys. **7**, 485 (2011).
[34] J. K. Glasbrenner, J. P. Velev, I. I. Mazin, Phys. Rev. B **89**, 064509 (2014).
[35] I. Paul, Phys. Rev. Lett. **107**, 047004 (2011).
[36] I. Paul, A. Cano, and K. Sengupta, Phys. Rev. B **83**, 115109 (2011).
[37] R. M. Fernandes *et al.*, Phys. Rev. Lett. **105**, 157003 (2010).
[38] F. Wang, H. Zhai, D.H. Lee, Phys. Rev. B **81**, 184512 (2010).
[39] M. J. Han and S. Y. Savrasov, Phys. Rev. Lett. **103**, 067001 (2009).
[40] P. Singh, Phys. Rev. Lett **104**, 099701 (2010).
[41] Ming-Cui Ding, Hai-Qing Lin, Yu-Zhong Zhang, Phys. Rev. B **87**, 125129 (2013).
[42] K. Kubo, Phys. Rev. B **75**, 224509 (2007).
[43] S. Graser, T. A. Maier, P. J. Hirschfeld, D. J. Scalapino, New J. Phys. **11**, 025016 (2009).
[44] J. Zhang, R. Sknepnek, R. M. Fernandes, and J. Schmalian, Phys. Rev. B **79**, 220502(R) (2009).
[45] C. Liu *et al.*, Phys. Rev. B **84**, 020509(R) (2011).
[46] P. M. R. Brydon, Maria Daghofer, Carsten Timm, J. Phys.: Condens. Matter **23**, 246001 (2011).
[47] N.B. Perkins, N.M. Plakida, Theoretical and Mathematical Physics **120** (3), 1182 (1999).
[48] F. Mancini, N.B. Perkins, N.M. Plakida, Physics Letters A **284** (6), 286 (2001).
[49] G. Jackeli and N. B. Perkins Phys. Rev. B **65**, 212402 (2002).